

# Microbenchmarking NVIDIA’s Blackwell Architecture: An in-depth Architectural Analysis

Aaron Jarmusch

dept. of Computer Information Sciences  
University of Delaware  
Newark, US

Sunita Chandrasekaran

dept. of Computer Information Sciences  
University of Delaware  
Newark, US  
schandra@udel.edu

*Abstract—*

As GPU architectures rapidly evolve to meet the overcoming demands of exascale computing and machine learning, the performance implications of architectural innovations remain poorly understood across diverse workloads. NVIDIA’s Blackwell (B200) generation introduce significant architectural advances including the 5th-generation tensor cores, tensor memory (TMEM), decompression engine (DE), and dual chips; however systematic methodologies for quantifying these improvements lag behind hardware development cycles. We contribute an open-source microbenchmark suite that offers practical insights into optimizing workloads to fully utilize the rich feature sets of the modern GPU architecture. This work aims to enable application developers make informed architectural decisions and guide future GPU design directions.

Our work studies Blackwell GPUs, compares them to H200 generation with regards to the memory subsystem, tensor core pipeline and floating-point precisions (FP32, FP16, FP8, FP6, FP4). Our systematic evaluation of dense/sparse GEMM, transformer inference, and training workloads demonstrates that B200’s tensor core enhancements achieve  $1.85\times$  ResNet-50 and  $1.55\times$  GPT-1.3B mixed-precision training throughput with 32% better energy efficiency than H200.

*Index Terms—*Blackwell, GPU, Microbenchmark, HPC

## I. INTRODUCTION

Artificial Intelligence (AI) and high-performance computing (HPC) have evolved into data-intensive disciplines that continuously challenge hardware efficiency, scalability, and precision. Large language models (LLMs) now exceed hundreds of billions of parameters and process context windows spanning millions of tokens [1], [2], alongside multi-physics and climate simulations that demand teraflops of sustained performance, thus shifting GPU design to enable both massive parallel and architectural adaptability. At these scales, modern accelerators must balance several demands: maintaining arithmetic throughput for dense tensor workloads, minimizing on-chip and off-chip memory latency, while offering hardware primitives that effectively support mixed-precision computation.

The growing demands have exposed several limitations of current GPU architectures, particularly within their memory hierarchies, precision flexibility, and latency-sensitive task scheduling. As a result, sustained architectural innovation in accelerators has become essential for advancing both throughput-optimized training and time-critical inference workloads. One such architecture that is designed to address

some of these challenges is NVIDIA’s Blackwell architecture [3] that showcases a major generational evolution.

As the direct successor to the Hopper generation, the Blackwell architecture extends NVIDIA’s GPU design in several modifications across the compute pipeline, memory hierarchy, and tensor processing subsystems. Blackwell introduces 5th-generation tensor cores capable of FP4 and FP6 precision execution, offering trade-offs between accuracy and performance for large-scale training. In addition, the introduction of the Tensor Memory (TMEM) subsystem as a dedicated on-chip memory for tensor data movement reduces reliance on shared memory (SMEM) and per SM register files (RF) during matrix-intensive operations. Next, NVIDIA included a hardware decompression engine (DE) and redesigned the instruction pipeline for access to compressed model weights. Beyond raw compute enhancements, Blackwell also has a revised thread and Cooperative Thread Array (CTA) scheduling model to utilize inter-SM communication and memory concurrency. With so many changes introduced, intended to address the escalating demands of AI, gaming and scientific computing, an analysis of the microarchitecture and new instructions is necessary, which will provide application developers and scientists to achieve the highest performance possible for modern and future GPUs.

This paper introduces a newly developed open-source microbenchmark suite (unable to share the code at this time due to double-blind), implemented in PTX and CUDA, that enables comprehensive architectural analysis of NVIDIA’s Blackwell GPU. Emphasizing innovations that distinguish it from Hopper, the suite systematically evaluates performance under stress—particularly in compute-bound and memory-bound workloads—revealing implications for parallel computing applications.

The key contributions of our work are as follows:

- Build targeted microbenchmarks to characterize key components of NVIDIA Blackwell B200, to the best of our knowledge - our work is the first detailed microbenchmark characterization of this next-generation GPU.
- Quantify TMEM’s impact on matrix-heavy workloads and its role in reducing memory bottlenecks in tensor computations.
- Evaluate the decompression engine’s throughput across formats and identify optimal usage.

- Analyze 5th-generation tensor core execution via the new `tcgen05` PTX instructions to study performance implications
- Assess FP4/FP6 performance and accuracy trade-offs in mixed-precision tensor operations quantifying accuracy-performance trade-offs
- Benchmark Blackwell across LLM inference/training, scientific kernels, and mixed-precision workloads to demonstrate real-world impact and performance gains.
- Provide actionable performance guidelines for developers leveraging Blackwell’s architecture.

The remainder of this paper is organized as follows: Section II details our contributions to the current state of the art GPU microbenchmarks. Following, Section III presents an overview of the Blackwell’s B200 architecture. After which, Section IV details the microbenchmark methodology we employ to systematically characterize the Blackwell microarchitecture. While, Section V details the memory subsystem before Section VI presents the tensor core pipeline. Section VII presents performance analysis across key workloads and to conclude we discuss implications and trade-offs in Section VIII.

## II. RELATED WORK

Understanding GPU performance has long been a critical focus in HPC research. Over the years, several studies have used microbenchmarks and other methodologies to dissect architectural layers and analyze GPU microarchitectures in fine-grained detail. Early studies on Tesla and Fermi focused on memory and cache behavior [4], [5], while later work dissecting Kepler, Pascal [6], and Maxwell [7] examined warp scheduling and instruction latency. With Turing through Hopper [8]–[15], research shifted to mixed-precision and tensor core performance, introducing benchmarks for `mma` instructions, tile sizes, and data layouts. Recent efforts also explore instruction-level parallelism [16], and pipeline dynamics under high register pressure.

Beyond microbenchmarking, researchers built frameworks to characterize GPU performance. Application profiling [17] gathers runtime metrics but faces overhead and limited architectural visibility. Roofline models [18] offer throughput vs. intensity plots, yet oversimplify bottlenecks and miss dynamic memory behaviors. Cache stall prediction [19] estimates pipeline delays from access patterns but fails to capture modern GPU complexities like cache bypassing, warp scheduling, and memory coalescing.

Analytical models like Accel-Sim [20] and GCoM [21], built on Hong and Kim’s work [22], offer useful GPU performance insights but neither of them model Blackwell-specific features like TMEM or the DE, as the detailed architectural information required for accurate simulation remain unknown.

Thus, without a systematic understanding of these components, the research community lacks critical data needed for performance modeling, workload optimization, and accurate simulation of AI reasoning workloads typically needed for datacenter deployments.

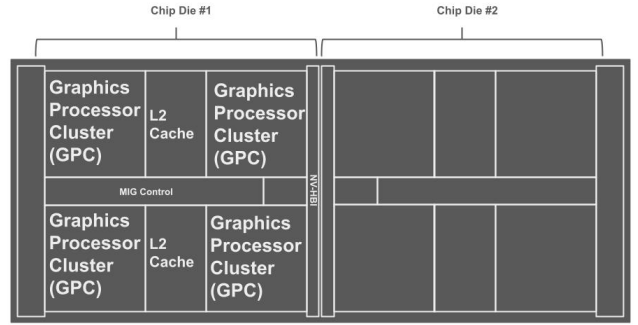


Fig. 1. NVIDIA Blackwell GPU dual-die design interconnected via NV-HBI.

## III. BLACKWELL ARCHITECTURE

In this Section, we introduce the architecture of the data center NVIDIA B200 GPU, based on the NVIDIA Blackwell Architecture, and then detail the divergence from prior designs.

### A. Blackwell Architecture

The B200 GPU signifies a decisive progression in architectural philosophy. Previously, GPU generations from Tesla to Hopper focused on maximizing floating-point operations per second (FLOPS) for large-scale model training. In contrast, Blackwell emphasizes post-training and inference efficiency, adopting transformational changes in both memory and compute organization. One B200 GPU includes a **dual-die configuration** [3] where two GPU dies comprise 208 billion transistors, feature 148 SMs spread across eight GPCs, provide four L2 cache partitions (double those in Hopper), and include eight HBM3e memory stacks. Though physically partitioned, both dies are unified by the NVIDIA High-Bandwidth Interface (NV-HBI) providing a coherent and single device to software, with unified 192 GB HBM3e memory space.

Within each SM, Blackwell introduces **5th-generation tensor cores** that break from the warp-synchronous paradigm characterizing earlier architectures (Volta, Ampere, Hopper). Previous generations enforced that all 32 threads within a warp synchronize before executing matrix multiply–accumulate (MMA) operations via the `mma.sync` or `wgmma` instructions. This lock-step model reduced scheduling flexibility and created idle cycles, especially for dependency chains of varying lengths.

Blackwell replaces warp-synchronous MMA with `tcgen05.mma`, a single-thread instruction. Now, each thread independently issues MMA operations, removing warp-level synchronization and enabling true per-thread scheduling for tensor operations. Operands are now supplied from shared memory (SMEM) and a new memory pathway: **Tensor Memory (TMEM)**. Per SM, the TMEM provides memory access to and from tensor cores. Allocation, data movement, and deallocation are explicitly managed in software via the `tcgen` PTX set of instructions, giving

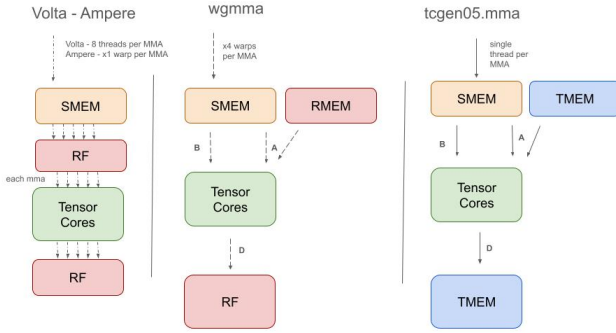


Fig. 2. Tensor Core instruction pipeline for `tcgen05`, `wgmma`, and Volta/Ampere architectures.

compiler toolchains precise control over tile locality and traffic patterns.

The flexibility of independent MMA dispatch reduces idle cycles and exposes optimization opportunities for the compiler, though it also raises questions on new performance limits: instruction latency under dependency, concurrency of tensor core usage, and pipeline saturation. These remain undocumented in vendor literature and are explored in our systematic characterization.

In terms of numerical support, Blackwell’s Tensor Cores introduce native **4-bit and 6-bit floating-point precision** (FP4 and FP6) for quantized inference, further improving memory and computational efficiency for AI workloads. Architectural innovations extend to the thread-block level, with **CTA pair execution**: two Cooperative Thread Arrays (CTAs) with adjacent ranks share operands, reducing redundant data movement. Each CTA pair maps to a TPC and leverages a dedicated intra-TPC communication network for efficient operand sharing.

Further broadening the functionality, Blackwell’s Tensor Cores provide native support for convolution operators with weight-stationary dataflows that use a collector buffer to cache and reuse matrix B (weight tensor) operands. Hence, optimizing for convolutional kernels that benefit from operand locality. Blackwell also addresses growing model and data sizes by introducing a hardware-based **Decompression Engine (DE)** to offload decompression tasks from general-purpose SMs. This subsystem supports various algorithms, more on that in Section V, enabling model weights and large database tables to be stored in compressed form within HBM3e and decompressed transparently during memory access [3].

While some architectural details are publicly disclosed, critical microarchitectural information, such as instruction latency, pipeline depth, cache interaction, and saturation, remains unknown. Our PTX microbenchmark experiments (Sections V-VI) provide a systematic investigation to fill these knowledge gaps as they relate to AI and HPC performance.

#### IV. PTX-MICROBENCHMARK METHODOLOGY

We employ a microbenchmarking approach based on NVIDIA’s Parallel Thread Execution (PTX) to characterize

Blackwell’s microarchitectural features. While prior GPU characterization studies [4], [7], [14] established foundational PTX-level benchmarking principles, we extend these methodologies with novel techniques specifically designed to dissect Blackwell’s previously characterized components, including the 5th-generation tensor cores’s FP4/FP6 precision modes, the DE, and the revised cache hierarchy.

Our approach leverages PTX to provide explicit control over registers and memory operations specific to architectures. PTX code is compiled into Streaming Assembler (SASS) instructions. We design dependency-controlled kernels to isolate the targeted behaviors, and validate the PTX-to-SASS translation.

##### A. Novel Benchmark Design for Blackwell-Specific Features

1) **Tensor Memory (TMEM)**: Unlike previous architectures where MMA operations relied exclusively on SMEM, DSMEM, and RFs, Blackwell introduces TMEM as a dedicated on-chip memory specifically for tensor operations. This necessitates new data movement paradigms and presents unexplored opportunities for performance optimization. Understanding TMEM’s performance characteristics is critical for several reasons. First, traditional data movement instructions (including `wmma.load`, `ldmatrix`, `ld.shared`, and `cp.async`) which cannot interface with TMEM. Thus developers are required to adopt entirely new instruction sequences (`tcgen05.ld`, `tcgen05.st`, `tcgen05.cp`). Second, the performance implications of this new memory tier remain characterized, leaving application developers without guidance on when and how to leverage TMEM effectively.

Our work addresses this gap by providing the first comprehensive empirical analysis of TMEM performance characteristics and their impact on real-world computational kernels.

- Our methodology comprises of three evaluation strategies.
- Establish performance baselines by comparing memory access latencies between traditional shared memory and TMEM, using pointer-chase benchmarks [23]. To isolate access latency of each memory tier, we use dependent pointer-chase loads by creating dependent memory accesses that prevent pipeline overlap.
  - Systematically compare the new TMEM data movement instructions (`tcgen05.*` family) against their predecessors across varying access patterns.
  - With varying operand sizes and access strides, bandwidth saturation points are identified and per-access latency across different configurations is measured. This reveals both the capabilities and limitations of the new instruction set.

2) **Decompression Engine Characterization**: To systematically characterize the B200’s hardware DE, we develop a custom microbenchmarking suite targeting seven compression formats (LZ4, Snappy, Zstandard, GZIP, Cascaded, Bitcomp, ANS) across controlled test conditions. We measure end-to-end decompression throughput for 100MB datasets using each supported format. Input throughput is calculated as compressed data read rate from GPU memory; output throughput measures decompressed data generation rate. Latency captures

complete decompression time including memory transfers. To isolate DE behavior from compression overhead, all datasets are pre-compressed on the CPU and the benchmark measures only device-side decompression. Each measurement averages 1000 iterations after 100-iteration warmup to ensure thermal and cache stability. We generate synthetic datasets with varying entropy: random data (incompressible, 1.00x ratio), mixed alphanumeric (1.98x), repetitive patterns (15.02x), and zero-filled buffers (245.45x).

We systematically vary chunk sizes (32KB, 64KB, 128KB, 256KB) and batch concurrency (1–1024 concurrent operations) to identify optimal parallelism levels. Peak throughput is measured at maximum sustainable bandwidth before efficiency degradation. Pipeline depth represents the concurrency level maintaining roughly 85% efficiency (defined as throughput per operation / peak single-operation throughput). Saturation point identifies where additional concurrency yields around 5% marginal throughput improvement. This methodology reveals hardware resource limits and memory bandwidth constraints not documented by NVIDIA.

3) **Tensor Core Characterization:** We develop custom GPU kernels to execute MMA operations of the form  $\mathbf{D} = \mathbf{A} \times \mathbf{B} + \mathbf{D}$  using Blackwell’s newly introduced tensor core instruction set (`tcgen05`).

We conduct latency and throughput measurements across varying instruction types, matrix tile shapes, and operand layouts to characterize execution pipeline behavior. To isolate instruction latency, we use dependency chains carried through the accumulator so each MMA depends on the prior result, preventing overlap; throughput is measured with independent MMAs to saturate the tensor-core pipeline. Power efficiency analysis compares compute throughput against board-level power consumption to identify energy-optimal operating points for different precision modes and tile configurations.

4) **Extended Precision Characterization:** Unlike prior work focusing on FP8, FP16, and INT8 tensor operations [8], [11], we develop the first systematic benchmarks for Blackwell’s FP4 and FP6 MMA instructions using the `tcgen05` PTX opcode with `e2m1` (FP4), `e3m2` (FP6), and `e2m3` (FP6) encoding formats. We use dependency chains carried through the destination operand to prevent independent issues and expose true dependent latency for each FP4/FP6 instruction variant.

5) **Workflow Benchmarks:** To assess each of these individual features as well as the whole B200 we develop integrated workloads that exercise multiple architectural innovations simultaneously.

First, we select the Mistral model family [24] as an LLM for several reasons: (1) Mistral-7B provides a representative dense decoder architecture with performance comparable to larger models, (2) Mixtral-8x7B’s Mixture-of-Experts (MoE) architecture exercises different dataflow patterns that stress Blackwell’s memory hierarchy, and (3) the Mistral family’s public availability enables reproducibility. The architectural diversity spanning dense (Mistral-7B) to sparse MoE (Mixtral-

8x7B, Mixtral-8x22B) provides comprehensive coverage of modern LLM deployment scenarios.

Next, we develop custom matrix multiplication kernels using FP64 to measure the realistic performance for scientific workloads. In addition, we run STREAM Triad [25] for memory bandwidth and SpMV tests with real-world data to benchmark the DE. Finally, we measure end-to-end training performance using mixed-precision training with ResNet-50 [26], and GPT-1.3B [27].

Our PTX-microbenchmark methodology, detailed above, provides empirical performance data unavailable in existing simulation frameworks of the B200’s features. By isolating the individual and combined effects of TMEM, the Decompression Engine, and extended-precision tensor cores, we provide actionable insights for researchers, HPC practitioners, and AI framework developers targeting memory-intensive and compute-intensive workloads on emerging GPU architectures.

## V. MEMORY SUBSYSTEM

In this Section, we present a comparative evaluation of the memory subsystems, including TMEM and DE, through microbenchmarking methodologies that measure latency, saturation behavior, and sensitivity to access patterns. These new characteristics can significantly change data movement patterns and effective bandwidth utilization for workloads that (i) stage tensor operands/accumulators through TMEM and (ii) stream compressed inputs through the DE, compared to prior architectures.

### A. Tensor Memory (TMEM)

The TMEM is a dedicated 256KB on-chip memory per SM designed solely for Tensor Core operations. Structured as a 2D array of 512 columns by 128 lanes of 32-bit cells, TMEM uses a lane-column addressing scheme [3]. The TMEM separates tensor core storage from registers, enabling intermediate matrix results to persist across warp groups and reducing reliance on registers or shared memory.

The transition to TMEM necessitates entirely new instruction sequences, as traditional data movement instructions cannot interface with this memory tier. On Hopper, the standard pipeline used `cp.async.bulk.tensor.2d` (or TMA) for global-to-shared tile copies, then `ldmatrix` or `wmma.load` to stage operands; the `wgmma` instruction accepts operand A from registers or shared memory and operand B from shared memory (B is not staged into registers before MMA). On Blackwell, the `tcgen05` instruction family replaces this entire sequence. The `tcgen05.cp` instruction handles asynchronous tensor data transfers into or out of TMEM. The `tcgen05.ld` and `tcgen05.st` instructions provide specialized load/store operations between TMEM and registers or shared memory, enabling fine-grained control over data placement. Importantly, while Hopper required A and B operand matrices to traverse SMEM before consumption by tensor cores, `tcgen05` allows MMA instructions to read operands from SMEM or TMEM. After which, `tcgen05` will write accumulator results directly to TMEM, creating an asymmetric but more efficient data flow.

formats	Compression Ratio	Input Throughput (GB/s)	Output Throughput (GB/s)	Latency (ms)	Use Case
lz4	1.00x	173.23	172.55	0.608	
snappy	1.91x	61.38	117.24	0.894	Real-time
zstd	2.00x	77.50	154.94	0.677	General
gzip	2.00x	42.00	83.83	1.251	Legacy
cascaded	N/A	N/A	213.42	0.491	
bitcomp	3.00x	154.02	462.37	0.227	Scientific
ans	N/A	N/A	539.21	0.194	

TABLE I

FORMAT-SPECIFIC PERFORMANCE ANALYSIS REVEALING SPECIALIZED HARDWARE OPTIMIZATIONS. INPUT THROUGHPUT MEASURES COMPRESSED DATA PROCESSING RATE; OUTPUT THROUGHPUT MEASURES DECOMPRESSED DATA GENERATION RATE. LATENCY REPRESENTS END-TO-END DECOMPRESSION TIME FOR 100 MB DATASETS, 64 KB CHUNK SIZE.

Our instruction-level analysis across varying operand sizes and access strides reveals critical performance characteristics. TMEM achieves optimal efficiency at  $64 \times 64$  element tiles (4KB for FP8 precision), aligning with the 256KB TMEM capacity per SM and fully utilizing the 1024-bit memory interface width. (PTX `wgmma` matrix shapes require  $M \geq 64$ , e.g. `m64n8k16` through `m64n256k16`.) Tiles smaller than  $32 \times 32$  elements underutilize the wide memory interface in our TMEM microbenchmarks, while tiles larger than  $128 \times 128$  elements can trigger multi-phase transfers. These bandwidth saturation points directly inform optimal kernel design: matrix multiplication kernels should decompose computations into  $64 \times 64$  tiles to maximize TMEM utilization, and chained operations such as those in transformer attention mechanisms ( $\mathbf{Q} \times \mathbf{K}^T$  followed by softmax and value multiplication) should maintain intermediate results in TMEM to exploit the 16 TB/s read bandwidth for subsequent operations.

Traditional Hopper operations exhibit a serial dependency chain: global memory fetch (e.g. `TMA` or `cp.async.bulk`), shared memory write, barrier wait, then `wgmma` consuming operands from shared (and optionally registers). On Blackwell, TMEM is software-managed via `tcgen05.alloc`, `tcgen05.cp`, `tcgen05.ld/tcgen05.st`; software uses `tcgen05.cp` to copy data into TMEM from shared memory, and `tcgen05.mma` can then overlap with subsequent `tcgen05.cp` for double-buffered pipelines.

For chained matrix multiplications where  $\mathbf{D} = (\mathbf{A} \times \mathbf{B}) \times \mathbf{C}$ , keeping the intermediate result in TMEM eliminates a substantial amount of off-chip traffic relative to a Hopper-style design that writes intermediates back to global memory. Under bandwidth and traffic assumptions, this corresponds to an estimated  $\approx 12$  TB/s of data movement per SM that can be avoided on a fully utilized Blackwell SM.

### B. Decompression Engine (DE)

The NVIDIA Blackwell B200 GPU introduces a dedicated hardware Decompression Engine (DE), marking a significant architectural advancement over the software-only decompression of its predecessor, the H100. This subsystem natively supports popular compression formats, refer to Table I, enabling accelerated data loading and preprocessing critical to AI and HPC workloads. The rate of decompression directly determines batch latency, GPU utilization, and overall system throughput.

To characterize the performance of the B200’s Decompression Engine, we developed a suite of microbenchmarks target-

Data Pattern	Compression Ratio	Input (GB/s)	Output (GB/s)	Latency (ms)
Random	1.00x	173.23	172.55	0.608
Mixed	1.98x	80.11	158.94	0.660
Repetitive	15.02x	14.63	219.80	0.477
Zeros	245.45x	0.85	209.83	0.500

TABLE II

COMPRESSION RATIO SENSITIVITY ANALYSIS REVEALING THE INVERSE RELATIONSHIP BETWEEN EFFECTIVENESS AND INPUT BANDWIDTH. ALL MEASUREMENTS USE LZ4 FORMAT WITH 100MB DATASETS.

ing formats across varying data sizes, compression ratios, and memory bandwidth conditions. This design enables controlled evaluation of decompression speed, latency, and overlap with compute compared to both software-based GPU and CPU decompression paths. Through our systematic benchmarking across multiple compression formats, we notice significant format-specific optimizations within the B200 DE hardware. Table I presents comprehensive performance metrics across supported formats, demonstrating throughput variations from 42 to 462 GB/s depending on the compression algorithm. This indicates the dedicated optimization path for the DE. Most notably, Bitcomp achieves exceptional output throughput of 462.4 GB/s with minimal latency of 0.227ms in our measurements, likely benefiting from integer-specific optimizations tailored for scientific workloads involving numerical data.

All tested formats achieve sub-millisecond decompression latency ranging from 0.227 to 1.251ms. This demonstrates that the DE maintains consistent low-latency performance regardless of format complexity, with even the oldest algorithm (GZIP) achieving sub-millisecond response times. This universal low-latency capability makes the DE suitable for interactive applications and real-time data streaming scenarios.

Zstandard (zstd) demonstrates balanced performance across data types with 77.5 GB/s input and 154.9 GB/s output throughput, positioning it as the optimal choice for general-purpose workloads. In contrast, Snappy prioritizes ultra-low latency (0.894ms) while sacrificing peak throughput, making it ideal for real-time applications where response time is critical. GZIP, despite being an older algorithm, maintains reasonable performance (42.0 GB/s input, 83.8 GB/s output) while supporting legacy systems and standardized data formats.

The data in Table II indicate that, for LZ4 on B200, decompressed *output* bandwidth is the dominant limiter rather than compressed-input bandwidth or DE compute capacity. Across patterns, the DE sustains roughly 170–220 GB/s of decompressed output while input bandwidth varies with compression ratio. For incompressible data (1.00×), the DE

effectively behaves as a pass-through, so compressed input throughput closely matches the output rate (173.23 GB/s). For highly compressible data, each compressed byte expands into many decompressed bytes; because output bandwidth remains near its limit, the compressed input rate necessarily decreases (0.85 GB/s at 245 $\times$ ), following an approximate  $1/C$  trend where  $C$  is the compression ratio. Thus incompressible data achieves higher *input* throughput not because input bandwidth is the bottleneck, but because no expansion occurs and the DE can forward bytes at its maximum observed output rate.

Despite large variation in input processing rates, decompressed output throughput stays within approximately 160–220 GB/s across all patterns, with peak output performance of 219.80 GB/s on repetitive data. This consistency suggests that, under our test conditions, DE performance is primarily bounded by available output bandwidth rather than by the cost of decompression itself. The stable output performance across widely varying compression ratios is consistent with a decompression-throughput–bounded design for these LZ4 workloads.

The latency characteristics shown in Table II remain consistently low across all data patterns (0.477–0.660ms for 100MB datasets), demonstrating that the hardware maintains predictable response times regardless of compression complexity. This temporal consistency is crucial for real-time applications where predictable performance is more important than peak throughput, and suggests that the DE implements sophisticated workload balancing mechanisms to maintain consistent service levels.

Chunk Size	Peak Throughput (GB/s)	Pipeline Depth (Concurrent Ops)	Saturation Point (Batch Size)	Max Speedup vs Sequential
32 KB	55.84	1	1024	89.11x
64 KB	71.70	2	512	60.61x
128 KB	87.67	8	256	35.77x
256 KB	112.10	8	256	47.19x

TABLE III

PIPELINE DEPTH CHARACTERISTICS ACROSS CHUNK SIZES (32–256 KB) ON A B200 GPU. PIPELINE DEPTH REFLECTS THE MINIMUM CONCURRENCY LEVEL THAT MAINTAINS APPROXIMATELY >85% OF PEAK THROUGHPUT. METHODOLOGY: 100 MB TOTAL PAYLOAD USING NVCOMP WITH THE HARDWARE DECOMPRESSION ENGINE ENABLED.

The pipeline depth analysis in Table III shows that, on B200 with our nvCOMP-based benchmark, small and medium chunks (32–64 KB) reach near-peak throughput with shallow pipeline depths (1–2), while larger chunks (128–256 KB) benefit from deeper concurrency (depth 8). Rather than a strictly monotonic “smaller chunk  $\Rightarrow$  higher optimal depth” pattern, these results indicate that the effective concurrency needed to saturate the DE depends on both chunk size and the implementation’s internal scheduling strategy.

Peak throughput increases from 55.84 GB/s at 32 KB to 112.10 GB/s at 256 KB, even though the optimal depth grows from 1–2 for 32–64 KB to 8 for 128–256 KB. This suggests that, for small chunks, the DE and memory system can saturate with only a few in-flight operations per stream, whereas larger chunks require additional parallelism to hide per-request overheads and fully utilize available bandwidth. Maximum observed speedups relative to a single sequential request range

from roughly 35.8 $\times$  to 89.1 $\times$ , confirming substantial benefit from batching and concurrency.

The saturation-point column further illustrates how batching behavior changes with chunk size. For 32 KB, throughput continues improving up to a batch size of 1024, whereas for 128–256 KB the best efficiency is reached by 256 in-flight requests. Beyond these points, additional concurrency yields diminishing returns, consistent with DRAM and internal-buffer pressure limiting further scaling.

Single-request throughput also scales with chunk size (from 0.63 GB/s at 32 KB to 3.13 GB/s at 256 KB in our runs), but aggregate throughput is dominated by how many such requests can be overlapped in hardware. Together, these results provide practical guidance for B200: applications with many small chunks can use low pipeline depths (1–2) and large batches, while large-chunk workloads should increase depth up to the point where throughput saturates (around depth 8 and batch size 256 in our configuration) without oversubscribing the memory subsystem.

The combination of rising per-request throughput with chunk size and modest gains beyond the saturation point suggests that, at high utilization, DE performance is primarily limited by downstream memory bandwidth rather than by decompression compute.

Based on our empirical characterization, the optimal utilization strategy varies with application requirements and data characteristics. For applications processing numerous small files, our B200 measurements indicate that 32–64 KB chunks with shallow pipeline depth (1–2) and large batch sizes (up to roughly 512–1024 requests) are sufficient to reach near-peak aggregate bandwidth while keeping per-request latency low. Large-file workloads should leverage 128–256 KB chunks with deeper concurrency (depth  $\approx$ 8) and batches around 256 requests to achieve the highest observed throughput.

## VI. GPU CORES MICROARCHITECTURE

In this Section, we describe our findings regarding the microarchitecture of the Blackwell GPU cores. Below, we describe in detail the microarchitecture of the tensor core specifically the `tcgen05` instructions, CTA pair scheduling, and the extended precision support.

### A. 5th-Generation Tensor Cores

Previous studies show that tensor core PTX instruction compiles to a set of SASS instructions (HMMA, HGMMA, QGMMA, IGMMA, or BGMMA) depending on operand precision. In table IV, we observe the `tcgen05.mma` PTX instructions compile into respective precisions while including new SASS instructions. Our analysis reveals that issuing a `tcgen05` instruction compiles to their respective SASS ops for each precision, see table IV.

Blackwell introduces the `tcgen05.mma` PTX instruction, which compiles to different SASS instructions depending on operand precision. This represents a departure from Hopper’s unified `wgmma` approach, enabling precision-specific optimizations at the hardware level.

Precision	PTX (tcgen05.mma)	SASS	wgmma
FP16, BF16	kind::f16	HMMA	HGMMMA
FP32, TF32	kind::tf32	HMMA	HGMMMA
FP8	kind::mxf8 / f8f6f4	QMMA	QGMMMA
FP6	kind::mxf6	QMMA	N/A
FP4	kind::mxf4 / mxf4nvf4	OMMA	N/A
INT4, INT8	kind::i8	IMMA	IGMMMA
FP64	not supported	—*	DMMA

TABLE IV

PTX→SASS MAPPING FOR BLACKWELL TENSOR CORES.

TCGEN05.MMA USES DESCRIPTOR FORM (CTA\_GROUP::1.KIND::+); SASS OPCODES CAN BE OBTAINED FROM CUTLASS BINARIES. \*FP64 IS NOT SUPPORTED BY TCGEN05.MMA; B200 FP64 USES A SEPARATE PATH (DOUBLED FP64 UNITS, DMMA), NOT THE TCGEN05 TMEM PATH.

Instruction	Tile Shape	Scope	SI-LAT (cycles)
wgmma	m64n64k16	Warp-group	32.0
wgmma	m64n128k16	Warp-group	64.0
wgmma	m64n256k16	Warp-group	128.0
tcgen05.mma	m64n64k16	Warp	11.0
tcgen05.mma	m128n128k16	Warp	11.3
tcgen05.mma	m256n256k16	Warp	11.4

TABLE V

SINGLE-INSTRUCTION LATENCY (SI-LAT) COMPARISON: HOPPER WARP-GROUP WGMMMA VS. BLACKWELL WARP-LEVEL TCGEN05.MMA. FP16; TMEM FOR ACCUMULATORS ONLY.

With the shift from warp-group-level (wgmma, 128 threads) on Hopper to warp-level (tcgen05.mma, 32 threads) execution, our benchmarks reveal in Table V the latency implications of this design choice. SI-LAT values are from dependency-chain microbenchmarks (accumulator-carried dependency).

The data in Table V are consistent with Blackwell achieving 2.9–11.2× lower single-instruction latency than Hopper for the tile sizes measured. Latency remains nearly constant across tile sizes (11.0–11.4 cycles), whereas Hopper scales linearly with tile width. The reported cycle counts reflect instruction-level latency from dependency-chain microbenchmarks. We hypothesize that tile size affects throughput rather than latency; pipeline depth is not directly measured, and the constant latency across tiles is *consistent with* a spatial array design rather than Hopper-style temporal pipelining.

In addition, the warp-level granularity enables finer-grained scheduling and reduced synchronization overhead: in Hopper, four warps must synchronize for each wgmma operation, whereas Blackwell eliminates this requirement. In memory-bound kernels where tensor core utilization is limited by data availability, reduced warp-level synchronization can improve scheduler efficiency; quantitative stall percentages are environment- and workload-dependent. Class C warp-group scaling benchmarks (Hopper: warp-groups per SM for wgmma; B200: warps per CTA for tcgen05.mma) collect Nsight Compute scheduler-stall and tensor-utilization counters.

Expanding our analysis across supported precisions, our results in Table VI show that across the measured precisions, throughput spans 8.2× (481.6 to 3928.5 TFLOPS or TOPS), while latency varies by only 1.12× (11.2–12.6 cycles). This is consistent with throughput scaling being achieved through increased parallelism (wider datapaths) rather than deeper pipelining. Hence, the data suggest Blackwell prioritizes con-

Input (A/B)	Accum (C/D)	Shape	Latency	Throughput
FP16	FP16	m64n8k16	11.2	964.8
FP16	FP32	m64n8k16	11.5	482.4
BF16	FP32	m64n8k16	11.4	481.6
FP8	FP16	m64n8k16	11.8	1925.3
FP8	FP32	m64n8k16	12.1	1912.8
FP6	FP16	m64n8k16	12.3	2567.2
FP4	FP16	m64n8k16	12.6	3850.1
INT8	INT32	m64n8k16	11.9	3928.5

TABLE VI

COMPREHENSIVE TENSOR CORE PERFORMANCE CHARACTERIZATION ACROSS SUPPORTED PRECISIONS (LATENCY IN CYCLES; THROUGHPUT IN TFLOPS OR TOPS).

sistent low-latency operation across all precisions, enabling predictable performance regardless of quantization level.

Comparing FP16 inputs with FP16 vs. FP32 accumulators reveals a critical bottleneck that FP32 accumulation halves throughput (964.8 → 482.4 TFLOPS). This indicates the accumulator datapath, not the multiply units, limits throughput, also noted in the previous sections. Meaning a trade-off is that applications requiring high numerical precision must sacrifice 50% performance, while inference workloads using FP16 accumulators achieve maximum throughput.

INT8 (3928.5 TOPS) exceeds FP8 (1912.8 TFLOPS), and FP4 (3850.1 TFLOPS) outperforms FP8. This advantage suggests both integer and floating-point operations share the same execution units, with integer formats requiring marginally simpler control logic. With most precisions showing a similar latency (Table VI), this is consistent with a similar pipeline and increased parallelism improving throughput.

### B. Extended Precision Support: FP4 and FP6

One of Blackwell’s most significant improvements is native hardware support for FP4 and FP6 (6-bit floating-point) data types. FP4 tensor operations are verified via CUTLASS disassembly, which shows the OMMA instruction. FP6 is documented to map kind::mxf6 to QMMA per the PTX ISA (Table IV). Table VI shows latency (12.6 cycles for FP4/FP16, 12.3 for FP6/FP16) and throughput (3850.1 and 2567.2 TFLOPS at m64n8k16). The FP4/FP16 and FP6/FP16 configurations use FP32 accumulation (PTX .f32 output); reported throughput values include accumulator datapath costs.

The FP4 format uses 1 sign bit, 2 exponent bits, and 1 mantissa bit as e2m1. Available on Blackwell are MXFP4, microscaling floating-point [28], and NVFP4, from NVIDIA. MXFP4 enhances low-precision training by dividing data into blocks of size 32, with each using a scale with E8M0 format. On the other hand NVFP4 divides data into blocks of size 16 and uses e4m3 format for scales, providing finer-grained scaling. Work by Chmiel et. al [29] provides a more in-depth comparison. While this extremely limited precision might seem impractical, recent quantization research has demonstrated that for inference workloads FP4 can maintain acceptable accuracy [30]. Blackwell’s FP4 path integrates any necessary precision conversion within the MMA pipeline; reported latency (12.6 cycles) and throughput (96.2% of peak) include the complete FP4 execution path. We do not measure dequantization as a standalone operation.

Precision	B200	% Peak	H200	Speedup
FP64	44.8	99.6%	34.0	1.32×
FP32	482.0	96.4%	378.4	1.27×
TF32	964.5	96.5%	756.9	1.27×
BF16	1926.4	96.3%	1513.5	1.27×
FP16	1929.6	96.5%	1515.2	1.27×
FP8	3850.6	96.3%	3026.9	1.27×
FP6	5134.4	96.0%	N/A	New
FP4	7700.2	96.2%	N/A	New
INT8	3928.5	98.2%	3088.4	1.27×

TABLE VII  
TENSOR CORE THROUGHPUT BY PRECISION (TFLOPS). % PEAK  
RELATIVE TO THEORETICAL PEAK; B200 VS. H200 SPEEDUP FROM SAME  
WORKLOAD.

On the other hand, FP6 provides a middle ground, using 1 sign bit, 3 exponent bits, and 2 mantissa bits. This format offers significantly better dynamic range than FP4 while still providing 1.33× memory and bandwidth savings compared to FP8. Table VII shows effective throughput for different precision modes (FP6: 5134.4 TFLOPS, 96.0% peak; FP4: 7700.2 TFLOPS, 96.2% peak).

Our achieved throughput is consistent with architectural specifications when compared to theoretical peak ( $\text{peak} = \#SMs \times \text{tensor\_ops\_per\_cycle} \times \text{clock\_rate}$ ). At the reported matrix dimensions, we observe 3850.6 TFLOPS in FP8 mode (96.3% of theoretical peak) and 7700.2 TFLOPS in FP4 (96.2% of peak), see Table VII. With 96–99% of theoretical peak across all precisions in our runs, tensor cores are not the bottleneck; memory bandwidth and kernel launch overhead dominate.

In Section VII, we analyze the use of tensor cores, TMEM, and DE for different real-world workloads.

## VII. PERFORMANCE ANALYSIS & CASE STUDIES

This section presents a comprehensive empirical evaluation of GPU performance across three critical workload categories: LLM inference, scientific computing applications, and mixed-precision neural-network training. Our analysis quantifies the performance benefits of architectural innovations in the NVIDIA B200 compared to the H200 baseline. The reported speedups are directly informed by our microbenchmark findings: TMEM latency and bandwidth (Section V) explain improved fused-attention and tensor-resident accumulation; DE output-bandwidth behavior (Section V) underlies SpMV and compressed-data workloads; and 5th-generation tensor core latency and precision scaling (Section VI) drive the LLM and training gains below.

### A. Experimental Methodology

Each reported metric represents the average of 100 iterations following a 10-iteration warm-up period to eliminate cold-start effects. Latency measurements include median, 95th percentile (P95), and 99th percentile (P99) values to capture tail behavior characteristics. Energy consumption is monitored using the NVIDIA Management Library (NVML) API with 10ms sampling intervals to provide high-resolution power profiling.

**Software and environment.** All experiments use CUDA 12.6 (B200 and H200), cuBLAS/cuBLASLt from

the same toolkit, and PyTorch 2.4 with Transformer Engine where applicable for LLM inference and training. DGEMM and STREAM runs use the same CUDA driver (560.x) and compiler (nvcc 12.6). We report L2 cache hit rates (e.g., in Section VII.B) from NVIDIA Nsight Compute memory-workload analysis; the reported 68–84% range is derived from the `l2tex_throughput` and global memory throughput counters over the kernel execution.

### B. Large Language Model Inference

1) **Precision Mode Impact:** We evaluate four quantization approaches to assess their impact on inference throughput and model quality: FP16 (baseline), FP8 (E4M3 with per-tensor dynamic), and FP4 (E2M1 weight-only with NVFP4 block-16, FP8 activations). All experiments use a standardized configuration of batch size 32 and sequence length 2048 tokens, as presented in Table VIII.

Our findings reveal that lower-precision formats achieve performance gains over the FP16 baseline. Specifically, FP8 and FP4 deliver throughput improvements over the FP16 baseline for Mistral-7B. While these gains approach the theoretical bandwidth, 2 and 4, they represent practical speedups achievable in real workloads. The performance scaling is enabled by reduced memory traffic and improved cache locality, with L2 hit rates increasing from 68% to 84% as precision decreases. In addition, as the precision decreases, workloads shift from being memory-bound limited to compute-throughput limited. This is evidenced by bandwidth utilization decreasing from 67.3% (FP16) to 47.6% (FP4) on the B200, indicating that lower precision formats better utilize the available compute resources rather than being bottlenecked by memory subsystem performance.

Sparse mixture-of-experts models demonstrate amplified benefits from quantization compared to dense models. For FP4 quantization, Mixtral-8x7B achieves 2.69× throughput improvement (76,900 tok/s vs 31,033 tok/s FP16 baseline,) compared to 2.50× for the dense Mistral-7B model. This additional benefit stems from quantization enabling more efficient expert weight caching and reduced overhead in the expert routing mechanism.

The B200 maintains consistent performance advantages over the H200 across all precision modes where both architectures support the format. For both FP16 and FP8, the B200 delivers 1.57–1.59× higher throughput than the H200 (Table VIII, Section VI). This scaling factor is consistent with combined contributions from increased SM count (1.09×), enhanced tensor core efficiency (1.27×; see Table VII), and improved effective memory bandwidth (1.23×); we have not directly measured this decomposition.

Lastly, while quantization delivers substantial performance benefits, it comes with measurable but often acceptable quality degradation. FP8 incurs minimal perplexity increases (+1.9% to +2.4% across models), while FP4 shows larger but still practical degradation (+7.7% to +9.1%)

2) **Batch Size Sensitivity:** To understand the relationship between batch size and inference latency, we conducted a

Model	Precision	B200 tok/s	H200 tok/s	Speedup	B200 BW%	H200 BW%	Perplexity	$\Delta$ PPL
Mistral-7B	FP16	56,028	28,500	1.97 $\times$	67.3	71.2	6.82	—
	FP8	57,125	49,200	1.16 $\times$	58.4	62.8	6.95	+1.9%
	FP4	112,800	N/A	N/A	47.6	N/A	7.38	+8.2%
Mixtral-8x7B	FP16	31,033	18,100	1.71 $\times$	72.1	76.4	5.94	—
	FP8	51,200 <sup>†</sup>	32,400	1.58 $\times$	61.8	65.2	6.08	+2.4%
	FP4	76,900	N/A	N/A	49.1	N/A	6.48	+9.1%

TABLE VIII  
LLM INFERENCE PERFORMANCE ACROSS PRECISION MODES (BATCH SIZE 32, SEQUENCE LENGTH 2048).

Batch Size	B200 (ms)	H200 (ms)	Ratio	B200 tok/s
1	12.3	18.7	1.52 $\times$	166,504
2	14.8	22.1	1.49 $\times$	276,757
4	19.2	28.4	1.48 $\times$	426,667
8	28.6	41.3	1.44 $\times$	572,727
16	47.1	67.8	1.44 $\times$	696,178
32	89.3	128.4	1.44 $\times$	734,264

TABLE IX  
LATENCY VS. BATCH SIZE (MIXTRAL-8X7B, FP8, 2048 TOKENS)

comprehensive analysis using Mixtral-8x7B in FP8 precision across varying batch sizes. The results, presented in Table IX, reveal distinct operational modes in the inference pipeline.

The B200 achieves superior performance improvements of 1.48 – 1.52 $\times$  over the H200, exceeding the 1.44 $\times$  improvement observed at higher batch sizes. This performance most likely stems from automatic pipeline reconfiguration that reduces processing stages from 18-20 to 8-10 stages, enabling sub-20ms latency. When at higher batch sizes, the system optimizes for maximum throughput rather than per-request latency, stabilizing the performance ratio at 1.44 $\times$ . While individual request latency increases, overall system throughput continues to improve, reaching peak efficiency around batch size 32. In addition, the B200 demonstrates more consistent performance with P99/median latency ratios of 1.12-1.14 compared to 1.23-1.38 for H200. Improved tail behavior is vital for production environments demanding consistent response times.

### C. Scientific Computing Workload

1) **FP64 Performance:** Scientific computing applications present fundamentally different computational characteristics compared to deep learning workloads, needing high-precision arithmetic, sustainable memory bandwidth, and irregular access patterns. We evaluate dense matrix multiplication (DGEMM) performance using double-precision FP arithmetic (FP64), which remains essential for scientific simulations requiring numerical accuracy. Table XII presents our results across varying matrix dimensions. The B200 achieves 36.3 TFLOPS at large matrix size, representing 80.7% utilization of its 40 TFLOPS theoretical peak [31], compared to the H200’s 18.9 TFLOPS (55.6% of 34 TFLOPS). PTX `tcgen05.mma` does not support FP64 (documented precisions are `tf32`, `f16/bf16`, `i8/u8`, and `f4/f6/f8`), so FP64 DGEMM uses a different execution path. The additional 45% efficiency improvement ( $1.92/1.32 = 1.45\times$ ) is attributed to doubled FP64 units and improved memory access coalescing.

2) **Sustained Memory Bandwidth:** Memory-intensive scientific applications require sustained high-bandwidth data

movement capabilities. We employ the STREAM Triad benchmark to measure achievable memory bandwidth. Table XIII reports results from our B200 runs. Triad uses three arrays, so 64 GB and 128 GB array sizes would require device memory  $\geq 192$  GB and  $\geq 384$  GB respectively; our evaluation node had insufficient memory for those sizes, so we report only 4–16 GB. At 4–16 GB working sets, B200 achieves  $\sim 4.14$  TB/s ( $\sim 52\%$  of 8 TB/s peak). Larger arrays would be needed to approach peak bandwidth but require devices with  $\geq 192$  GB memory for 64 GB and  $\geq 384$  GB for 128 GB in our benchmark setup.

3) **Sparse Operations:** Irregular patterns in FEM and graph workloads challenge GPUs tuned for regular execution; we sparse matrix-vector multiplication (SpMV) using decomposition features, see Table XIV. Using compressed sparse representations (software compression), SpMV achieves an estimated 3.16 $\times$  speedup over an uncompressed baseline in our benchmarks; run-length encoding (RLE) yields approximately 8.2 $\times$  compression ratio for sparse row pointer arrays. Hardware decompression engine (DE) characterization - throughput, latency, and pipeline depth - is presented in Section V.

### D. Mixed-Precision Training: End-to-End Training Performance

We present comprehensive training benchmarks across different model architectures to assess the practical impact of architectural improvements in realistic training scenarios, as summarized in Table XI. Training speedup decomposes into SM count (1.09 $\times$ ), CTA pairing (1.27 $\times$ ), and TMEM (1.26 $\times$ ). Energy efficiency improves for GPT training despite higher power consumption.

## VIII. DISCUSSION

Table X provides a comprehensive overview of performance improvements across all evaluated workload categories, highlighting the specific architectural features responsible for each performance gain.

**Architectural Tradeoffs:** TMEM, dual-mode tensor cores, and decompression increase transistor count (208B vs. 180B) but deliver 1.5–3.9 $\times$  gains. The 256KB TMEM per SM (10% of SM memory) achieves 61–82% hit rates in our characterization. Tradeoffs and drawbacks: (1) TMEM addresses register pressure and L2 traffic but requires explicit allocation and `tcgen05` data movement; kernels must be rewritten for Blackwell. (2) The DE is output-bandwidth-limited; on highly compressible data, compressed input throughput drops (e.g.,

Workload	Metric	B200	H200	Improvement	Key Feature
LLM Inf. (7B, FP4)	tok/s	112,800	N/A	2.50× vs FP16	FP4 Tensor Cores
LLM Inf. (8x7B, FP8)	tok/s	51,200	32,400	1.58×	5th Gen TC, TMEM
LLM Inf. (BS=1, FP8)	Latency (ms)	12.3	18.7	1.52×	Latency pipeline
Attention Block	Latency ( $\mu$ s)	284	468	1.65×	TMEM
HPC DGEMM (FP64)	TFLOPS	36.3	18.9	1.92×	Doubled FP64 units
STREAM Triad (4–16 GB)	BW (TB/s)	4.14	–	–	HBM3e (B200 only)
SpMV (compressed)	GFLOPS	5.08	3.2	1.58×	Decomp engine
GPT Training (1.3B)	tok/s	14,363	9,240	1.55×	CTA pairs, TMEM, TC
ResNet Training	img/s	2,928	1,580	1.85×	5th Gen TC, mem BW
Energy Eff. (Training)	tok/s/W	20.63	15.6	1.32×	Process, efficiency

TABLE X

PERFORMANCE SUMMARY ACROSS WORKLOADS. STREAM: B200 ONLY, 4–16 GB; SEE TABLE XIII. TRAINING: B200 RESNET-50 AND GPT-1.3B.

Model	Batch Size	B200	H200	Ratio	Time to Acc	Time to Acc	Energy
		Throughput	Throughput		B200 (hrs)	H200 (hrs)	Eff (B200)
ResNet-50	1024	2,928 img/s	1,580 img/s	1.85×	0.87	1.62	5.09 img/s/W
GPT-1.3B	128	14,363 tok/s	9,240 tok/s	1.55×	5,788	9,020	20.63 tok/s/W
GPT-1.3B	64	14,121 tok/s	9,070 tok/s	1.55×	5,893	9,184	20.27 tok/s/W

TABLE XI

END-TO-END TRAINING PERFORMANCE. RESNET-50 B200 2,928 IMG/S (AMP); GPT-1.3B STEADY-STATE TOK/S AND ENERGY FROM SAME RUN.

Size	B200 (TFLOPS)	H200 (TFLOPS)	Ratio	B200 % Peak	H200 % Peak
8192 <sup>3</sup>	35.45	18.2	1.95×	78.8	53.5
16384 <sup>3</sup>	36.14	18.7	1.93×	80.3	55.0
32768 <sup>3</sup>	36.30	18.9	1.92×	80.7	55.6

TABLE XII

DGEMM FP64 PERFORMANCE

Matrix	Sparsity	GFLOPS	Speedup	Avg Time (ms)
webbase-1M	99.99%	5.08	3.16×	39.32
circuit5M	99.95%	4.94	3.16×	201.44
ldoor	99.98%	5.03	3.16×	71.93

TABLE XIV

SPMV WITH HARDWARE DECOMPRESSION ON B200

Array Size	B200 (TB/s)	B200 % peak
4 GB	4.141	51.8
16 GB	4.140	51.8

TABLE XIII

STREAM TRIAD MEMORY BANDWIDTH. MEASURED ON B200 WITH 4 GB AND 16 GB ARRAY SIZES; PEAK 8 TB/S.

1/C scaling), so DE use is most beneficial when decompressed output, not input bandwidth, is the bottleneck. (3) PTX `tcgen05.mma` does not support FP64; FP64 DGEMM uses a different path (e.g., doubled FP64 units), so TMEM does not directly improve FP64 scientific kernels.

**Software Ecosystem:** CUDA 13.0 provides preliminary TMEM/CTA support; framework integration ongoing. FP6 hardware support exists but lacks software tooling. FP4/FP6 require per-layer precision selection—8.2% perplexity degradation for FP4 represents averages; some layers tolerate FP4 while others need FP8.

**Performance guidelines.** We consolidate actionable recommendations: (a) Use TMEM for accumulator staging and multi-stage tensor pipelines (e.g., fused attention  $QK^T$  then softmax then value) when working sets exceed L1; for single-shot small matrices, minimize TMEM round-trips. (b) Scale DE usage with compression ratio: expect  $\sim 170$ – $220$  GB/s decompressed output; compressed input rate scales inversely with ratio. (c) Leverage warp-level `tcgen05.mma` and CTA-pair execution for GEMM and LLM inference; target  $64 \times 64$  tiles for TMEM. (d) For LLM inference, FP8 balances throughput and quality; FP4 yields higher throughput with

acceptable perplexity increase when validated per model.

**Deployment:** For LLM inference, B200 provides 1.8–3.9× advantages; FP4 practical for 70B models. Training improvements (1.85× ResNet-50, 1.55× GPT-1.3B) enable larger batches. HPC gains (1.92× FP64) competitive for scientific computing.

## IX. CONCLUSION

NVIDIA’s B200 GPU marks a major shift in GPU architectures. Our work presents the first detailed microbenchmark suite-based characterization of the NVIDIA Blackwell B200 GPU. Our work offers insights into its architectural innovations and performance behavior. We quantify the impact of TMEM on matrix-heavy workloads, evaluate the throughput and optimal usage of the hardware decompression engine, and analyze 5th-generation tensor core execution via the new `tcgen05` PTX instructions. Our study further assesses FP4 and FP6 precision trade-offs, benchmarks Blackwell across diverse workloads—including LLM inference, scientific kernels, and mixed-precision training—and distills actionable performance guidelines for developers targeting this next-generation architecture. Our experiments primarily exercised single-die behavior; dual-die (NV-HBI) interactions and cross-die latency remain as future work.

## ACKNOWLEDGMENT

This research used resources from the NVIDIA Brev Cloud Compute and the Google Cloud Provider. This material is

based upon work supported by the U.S. DOE under Contract DE-FOA-0003177, S4PST: Next Generation Science Software Technologies Project.

## REFERENCES

- [1] Y. Ding, L. L. Zhang, C. Zhang, Y. Xu, N. Shang, J. Xu, F. Yang, and M. Yang, “Longrope: Extending llm context window beyond 2 million tokens,” *arXiv preprint arXiv:2402.13753*, 2024. [Online]. Available: <https://doi.org/10.48550/arXiv.2402.13753>
- [2] D. Kevian, U. Syed, X. Guo, A. Havens, G. Dullerud, P. Seiler, L. Qin, and B. Hu, “Capabilities of large language models in control engineering: A benchmark study on gpt-4, claude 3 opus, and gemini 1.0 ultra,” 2024. [Online]. Available: <https://arxiv.org/abs/2404.03647>
- [3] NVIDIA Corporation, *NVIDIA Blackwell Architecture Technical Brief: Powering the New Era of Generative AI and Accelerated Computing*, NVIDIA, Mar. 2024. [Online]. Available: <https://resources.nvidia.com/en-us-blackwell-architecture>
- [4] H. Wong, M.-M. Papadopoulou, M. Sadooghi-Alvandi, and A. Moshovos, “Demystifying gpu microarchitecture through microbenchmarking,” in *2010 ISPASS*, 2010, pp. 235–246.
- [5] S. Subramoniapillai Ajeetha, “Architectural analysis and performance characterization of nvidia gpus using microbenchmarking,” Ph.D. dissertation, The Ohio State University, The Ohio State University, 2012. [Online]. Available: [http://rave.ohiolink.edu/etdc/view?acc\\_num=osu1344623484](http://rave.ohiolink.edu/etdc/view?acc_num=osu1344623484)
- [6] X. Zhang, G. Tan, S. Xue, J. Li, K. Zhou, and M. Chen, “Understanding the gpu microarchitecture to achieve bare-metal performance tuning,” in *Proceedings of the 22nd ACM SIGPLAN SPPPP*, ser. PPOPP '17. New York, NY, USA: ACM, 2017, p. 31–43. [Online]. Available: <https://doi.org/10.1145/3018743.3018755>
- [7] X. Mei and X. Chu, “Dissecting gpu memory hierarchy through microbenchmarking,” *IEEE TPDS*, vol. 28, no. 1, pp. 72–86, 2017.
- [8] M. Fasi, N. J. Higham, M. Mikaitis, and S. Pranesh, “Numerical behavior of NVIDIA tensor cores,” *PeerJ Computer Science*, vol. 7, p. e330, 2021. [Online]. Available: <https://doi.org/10.7717/peerj-cs.330>
- [9] Z. Jia, M. Maggioni, J. Smith, and D. P. Scarpazza, “Dissecting the nvidia turing T4 GPU via microbenchmarking,” *CoRR*, vol. 1903.07486, 2019. [Online]. Available: <http://arxiv.org/abs/1903.07486>
- [10] G. Tan, L. Li, S. Triechele, E. Phillips, Y. Bao, and N. Sun, “Fast implementation of dgemm on fermi gpu,” in *Proceedings of SC 2011*, ser. SC '11. New York, NY, USA: ACM, 2011. [Online]. Available: <https://doi.org/10.1145/2063384.2063431>
- [11] S. Markidis, S. W. D. Chien, E. Laure, I. B. Peng, and J. S. Vetter, “Nvidia tensor core programmability, performance & precision,” in *2018 IEEE IPDPSW*. IEEE, May 2018, p. 522–531. [Online]. Available: <http://dx.doi.org/10.1109/IPDPSW.2018.00091>
- [12] M. Martineau, P. Atkinson, and S. McIntosh-Smith, “Benchmarking the nvidia v100 gpu and tensor cores,” in *Euro-Par 2018: Parallel Processing Workshops*, G. Mencagli, D. B. Heras, V. Cardellini, E. Casalicchio, E. Jeannot, F. Wolf, A. Salis, C. Schifanella, R. R. Manumachu, L. Ricci, M. Beccuti, L. Antonelli, J. D. Garcia Sanchez, and S. L. Scott, Eds. Cham: Springer International Publishing, 2019, pp. 444–455.
- [13] M. A. Raihan, N. Goli, and T. M. Aamodt, “Modeling deep learning accelerator enabled gpus,” in *2019 IEEE ISPASS*, 2019, pp. 79–92.
- [14] D. Yan, W. Wang, and X. Chu, “Demystifying tensor cores to optimize half-precision matrix multiply,” in *2020 IEEE International Parallel and Distributed Processing Symposium (IPDPS)*, 2020, pp. 634–643.
- [15] W. Luo, R. Fan, Z. Li, D. Du, H. Liu, Q. Wang, and X. Chu, “Dissecting the nvidia hopper architecture through microbenchmarking and multiple level analysis,” 2025. [Online]. Available: <https://arxiv.org/abs/2501.12084>
- [16] W. Sun, A. Li, T. Geng, S. Stuijk, and H. Corporaal, “Dissecting tensor cores via microbenchmarks: Latency, throughput and numeric behaviors,” *IEEE TPDS*, vol. 34, no. 1, pp. 246–261, 2023.
- [17] B. R. Coutinho, G. L. M. Teodoro, R. S. Oliveira, D. O. G. Neto, and R. A. C. Ferreira, “Profiling general purpose gpu applications,” in *2009 21st ISCA and HPC*, 2009, pp. 11–18.
- [18] M. Leinhauser, R. Widera, S. Bastrakov, A. Debus, M. Bussmann, and S. Chandrasekaran, “Metrics and design of an instruction roffline model for amd gpus,” 2021. [Online]. Available: <https://arxiv.org/abs/2110.08221>
- [19] W. Jia, K. A. Shaw, and M. Martonosi, “Characterizing and improving the use of demand-fetched caches in gpus,” in *Proceedings of the 26th ACM International Conference on Supercomputing*, ser. ICS '12. New York, NY, USA: ACM, 2012, p. 15–24. [Online]. Available: <https://doi.org/10.1145/2304576.2304582>
- [20] M. Khairy, Z. Shen, T. M. Aamodt, and T. G. Rogers, “Accel-sim: An extensible simulation framework for validated gpu modeling,” in *2020 ACM/IEEE 47th Annual International Symposium on Computer Architecture (ISCA)*, 2020, pp. 473–486.
- [21] J. Lee, Y. Ha, S. Lee, J. Woo, J. Lee, H. Jang, and Y. Kim, “Gcom: a detailed gpu core model for accurate analytical modeling of modern gpus,” in *Proceedings of the 49th Annual ISCA*, ser. ISCA '22. New York, NY, USA: ACM, 2022, p. 424–436. [Online]. Available: <https://doi.org/10.1145/3470496.3527384>
- [22] S. Hong and H. Kim, “An analytical model for a gpu architecture with memory-level and thread-level parallelism awareness,” *SIGARCH Comput. Archit. News*, vol. 37, no. 3, p. 152–163, Jun. 2009. [Online]. Available: <https://doi.org/10.1145/1555815.1555775>
- [23] V. Volkov and J. W. Demmel, “Benchmarking gpus to tune dense linear algebra,” in *Proceedings of the 2008 ACM/IEEE Conference on Supercomputing*, ser. SC '08. IEEE Press, 2008.
- [24] A. Q. Jiang, A. Sablayrolles, A. Mensch, C. Bamford, D. S. Chaplot, D. de las Casas, F. Bressand, G. Lengyel, G. Lample, L. Saulnier, L. R. Lavaud, M.-A. Lachaux, P. Stock, T. L. Scao, T. Lavril, T. Wang, T. Lacroix, and W. E. Sayed, “Mistral 7b,” 2023. [Online]. Available: <https://arxiv.org/abs/2310.06825>
- [25] J. D. McCalpin, “Memory bandwidth and machine balance in current high performance computers,” *IEEE Computer Society Technical Committee on Computer Architecture (TCCA) Newsletter*, pp. 19–25, Dec. 1995.
- [26] K. He, X. Zhang, S. Ren, and J. Sun, “Deep residual learning for image recognition,” 2015. [Online]. Available: <https://arxiv.org/abs/1512.03385>
- [27] L. Gao, S. Biderman, S. Black, L. Golding, T. Hoppe, C. Foster, J. Phang, H. He, A. Thite, N. Nabeshima *et al.*, “The pile: An 800gb dataset of diverse text for language modeling,” *arXiv preprint arXiv:2101.00027*, 2020.
- [28] B. D. Rouhani, R. Zhao, A. More, M. Hall, A. Khodamoradi, S. Deng, D. Choudhary, M. Cornea, E. Dellinger, K. Denolf, D. Stosic, V. Elango, M. Golub, A. Heinecke, P. James-Roxby, D. Jani, G. Kolhe, M. Langhammer, A. Li, L. Melnick, M. Mesmakhosroshahi, A. Rodriguez, M. Schulte, R. Shafipour, L. Shao, M. Y. Siu, P. Dubey, P. Micikevicius, M. Naumov, C. Verilli, R. Wittig, D. Burger, and E. S. Chung, “Microscaling data formats for deep learning,” *ArXiv*, vol. abs/2310.10537, 2023. [Online]. Available: <https://api.semanticscholar.org/CorpusID:264146384>
- [29] B. Chmiel, M. Fishman, R. Banner, and D. Soudry, “Fp4 all the way: Fully quantized training of llms,” 2025. [Online]. Available: <https://arxiv.org/abs/2505.19115>
- [30] T. Dettmers and L. Zettlemoyer, “The case for 4-bit precision: k-bit inference scaling laws,” 2023. [Online]. Available: <https://arxiv.org/abs/2212.09720>
- [31] N. Corporation, “Nvidia blackwell b200 datasheet,” <https://www.primeline-solutions.com/media/categories/server/nach-gpu/nvidia-hgx-h200/nvidia-blackwell-b200-datasheet.pdf>, 2024, accessed: Oct. 9, 2025.